Polymer 51 (2010) 4916–4927

Contents lists available at ScienceDirect

Polymer

journal homepage: www.elsevier.com/locate/polymer

# Shear-induced orientation in polymer/clay dispersions via *in situ* X-ray scattering

Laura M.C. Dykes [a], John M. Torkelson [a,b], Wesley R. Burghardt [a,b,*], Ramananan Krishnamoorti [c]

[a] Department of Chemical and Biological Engineering, Northwestern University, Evanston, IL 60208, USA
[b] Department of Materials Science and Engineering, Northwestern University, Evanston, IL 60208, USA
[c] Department of Chemical Engineering, University of Houston, Houston, TX 77204, USA

ARTICLE INFO

*Article history:*
Received 29 May 2010
Received in revised form
6 August 2010
Accepted 8 August 2010
Available online 13 August 2010

*Keywords:*
Polymer–clay nanocomposites
X-ray scattering
Rheology

ABSTRACT

We report *in situ* X-ray scattering measurements of shear-induced orientation in polymer–clay dispersions. Two different organically modified clays, montmorillonite and fluorohectorite, are dispersed in a low molecular weight, viscous polymer melt, facilitating studies at room temperature. Orientation measurements are performed in the flow-gradient plane, allowing characterization of both the average degree and direction of particle orientation during shear. In all cases, the orientation angle is finite, indicating systematic misalignment of the particle long axes relative to the flow direction. In concentrated fluorohectorite and montmorillonite dispersions, anisotropy and orientation angle are roughly independent of shear rate, and negligible relaxation is observed upon flow cessation. Conversely, a lower concentration montmorillonite sample exhibits orientation that is more responsive to shear flow, and partially relaxes upon flow cessation. In this sample, the orientation behavior is interpreted in light of rotational diffusion of the clay particles. This same sample exhibits oscillatory structural dynamics upon shear flow reversal, attributed to tumbling rotations of the disk-like clay particles in shear. Large-amplitude oscillatory shear is similarly demonstrated to be capable of inducing significant particle orientation; the degree of orientation is principally determined by the applied strain amplitude. Complementary measurements of rheological properties exhibit many characteristics commonly reported in polymer–clay nanocomposites. Based on the structural measurements reported here, the rheological phenomena are interpreted to arise from a combination of flow-induced particle orientation and rate- and time-dependent destruction or reformation of particle networks.



## 1. Introduction

Polymer nanocomposites have attracted considerable attention as advanced engineering materials. Addition of relatively small quantities of nanoscale fillers (often layered clays) has been demonstrated to favorably impact mechanical and barrier properties, thermal stability and flame retardance [1–4]. The possibility of novel physical phenomena due to nanoscale confinement and extraordinarily large interfacial area in well-dispersed nanocomposites has provided additional motivation for study [5]. End use properties of polymer–clay nanocomposites will depend on the microscopic structure developed during in nanocomposite synthesis or compounding, as well as in final product fabrication. In particular, both mechanical [6] and barrier [7] properties are predicted to depend on the orientation distribution of the dispersed anisotropic mineral phase. Understanding the structural dynamics of nanocomposites under flow is thus of extreme interest. While this paper focuses on polymer–clay systems, similar issues arise in other classes of polymer nanocomposites, for instance those incorporating graphene nanoparticles [8].

There is overwhelming evidence that processing flows promote orientation of dispersed clay particles in polymer nanocomposites [9–16]. These studies have all involved *ex situ* characterization of process-induced orientation, typically using X-ray scattering [9–11,13,14,16] and/or transmission electron microscopy (TEM) [9,12,13,15]. In one study, Galgali et al. demonstrated how processing-induced orientation impacts mechanical properties [16]. Such *ex situ* studies have generally found that the long axes of disk-like clay particles orient along the flow direction during processing, leading to a roughly 'parallel' orientation state in shear-dominated flows like injection molding.

The rheology of polymer–clay nanocomposites has been extensively studied, and numerous common themes have emerged [17]. Early rheological characterization of a variety of nanocomposite systems demonstrated enhanced low-frequency viscoelasticity,

* Corresponding author. Department of Chemical and Biological Engineering, Northwestern University, Evanston, IL 60208, USA. Tel.: +1 847 467 1401; fax: +1 847 491 3728.
*E-mail address:* w-burghardt@northwestern.edu (W.R. Burghardt).

0032-3861/$ – see front matter © 2010 Elsevier Ltd. All rights reserved.
doi:10.1016/j.polymer.2010.08.013

in particular the emergence of a solid-like plateau in storage modulus [18–24]. Ren et al. postulated that this solid character results from a mechanically percolated network of disk-shaped particles, and developed a geometric model demonstrating that such networks can form at rather low concentration in well-dispersed polymer–clay hybrids owing to the high particle aspect ratio [20]. It is now generally accepted that enhanced low frequency storage modulus reflects some sort of particle network structure, and, in fact, low frequency viscoelasticity is often taken to be an indicator of the degree of exfoliation/dispersion in polymer–clay nanocomposites [21,22,24–27]. The solid character reflected in the low frequency storage modulus is also manifested in yield stress phenomena at low shear rates [28,29].

Nonlinear rheological phenomena have also been widely investigated in nanocomposites. Although strain-hardening behavior was reported in large-amplitude oscillatory shear (LAOS) in an end-tethered nylon–clay hybrid [30], most nanocomposites have shown strong strain-thinning behavior in LAOS [25,31–33]. The application of LAOS induces structural changes in the sample, such that the linear moduli measured at small strain following LAOS are often dramatically suppressed [19,22,25,34,35]; this has frequently been attributed to flow-induced particle orientation, and the subsequent recovery in moduli with time attributed to disorientation [25,35].

Unidirectional shearing is also capable of inducing microscopic structural changes in nanocomposites. The failure of the Cox-Merz rule [31,32] (an empiricism relating steady viscosity measured in shear flow to complex viscosity measured in small-amplitude oscillation) is attributed to different structural states during the two measurements. Similarly to the effects of LAOS, steady shearing can also induce a significant drop in the linear dynamic modulus measured following flow cessation, which may then show recovery as a function of time [29,36–38]. The logarithmic time-dependence of such modulus recovery has been interpreted using concepts from soft glassy dynamics [35–37]. Gradual structural evolution following cessation of shear flow has also been studied using interrupted shearing protocols, in which flow is resumed (either in the same or reversed direction) after various periods of relaxation [23,24,29,36–40]. Finally, thixotropic characteristics of nanocomposites have been investigated by measuring time-dependent changes in viscosity upon changes in shear rate [29,38,40].

The rheological phenomena described above undoubtedly reflect a close coupling between flow-induced changes in fluid microstructure and the corresponding mechanical response. The concepts most frequently invoked to interpret rheological data are (i) flow-induced orientation of particles, and (ii) the breakdown of particle network structure. Attempts have been made to model rheological phenomena in terms of such structural features [39]. Of course, both mechanisms may act in parallel. As discussed by Vermant et al. [38], unraveling the impact of each of these structural features solely based on rheological measurements is a considerable challenge. This provides the central motivation for the present study, in which direct measurements of particle orientation in polymer–clay dispersions are conducted via *in situ* X-ray scattering.

There has been direct scattering evidence of flow-induced orientation in both steady shear [41] and LAOS [34,35] based on *ex situ* characterization of quenched solid samples (Particle orientation induced by extensional flow has also been studied in quenched samples [42]). However, there have been very few measurements of flow-induced orientation in polymer–clay dispersions using *in situ* scattering *during* shear. Schmidt and coworkers used SANS to study clay dispersions in aqueous PEO solutions [43]; Medellin-Rodriguez et al. used SAXS to study orientation in end-tethered nylon–clay nanocomposites induced in shear flow [44]; and Lele et al. studied orientation in polypropylene–clay nanocomposites in pressure-driven capillary flow [45]. Interestingly, two of these studies report evidence of *perpendicular* alignment of clay particles in shear (in which the clay particle normals tend to orient along the vorticity axis of shear flow) [43,44], in contrast to the overwhelming majority of *ex situ* studies on sheared or processed nanocomposites that suggest parallel orientation is the norm. In each of these cases, it could be that unusually strong coupling between polymer and particle dynamics (as manifested, for instance, in the strain-hardening rheology observed in end-tethered nylon nanocomposites [30]) may be responsible for this unusual result. *In situ* studies reported to date have been rather limited in scope, focusing on steady flows, and providing only limited ability to make time-resolved measurements of slow dynamic processes [44,45]. The capillary flow measurements of Lele et al. [45] are complicated not only by intrinsic inhomogeneity in shear rate, but also by the fact that X-ray scattering data are averaged over varying projections of the shear flow axes in different regions of the flow. Similar *in situ* studies of particle orientation in sheared aqueous clay dispersions using either neutron [46,47] or X-ray [48,49] scattering have, again, concentrated on steady flow. *In situ* X-ray diffraction has also been coupled with rheology to study polymer–clay intercalation processes, but under small-amplitude oscillatory shear conditions where flow-induced orientation should not be an issue [50].

Here we employ synchrotron-based X-ray scattering to study shear flow-induced orientation in polymer–clay dispersions. The samples used are idealized, in that the polymer matrix is a relatively low viscosity, room-temperature melt. This both simplifies the experimental conditions (removing, for instance, concerns of thermal degradation of the polymer), and reduces complexities associated with background viscoelasticity in the matrix. Given the preponderance of evidence for parallel particle orientation in shearing and shear-dominated flows of polymer–clay nanocomposites, we pursue orientation measurements within the flow-gradient (1–2) plane of shear flow. This geometry is particularly informative in that it allows measurements of both the degree and direction of particle orientation in the 1–2 plane. Finally, the short exposure times enabled by synchrotron radiation allow us to study dynamic orientation processes in real time. The measurements of particle orientation are coordinated with rheological testing (performed off-line), in order to explore the connections between structure and rheology.

## 2. Experimental

### 2.1. Materials

We have studied dispersions of two different organically modified clays: dioctodecyl dimethyl ammonium-modified montmorillonite and an octodecyl trimethyl ammonium-modified fluorohectorite. Procedures for organic modification of the clays by ion exchange with alkyl amines are described elsewhere [35,51]. Montmorillonite particles have a Gaussian distribution of diameters with a mean size of 400 nm and a full-width at half max of 70 nm. Fluorohectorite particles are larger, with a diameter $\sim$5 μm. In all cases, the dispersing fluid is a random copolymer of dimethylsiloxane and diphenylsiloxane, in a mole ratio of 95:5. Similar copolymer matrices have been used in prior studies of nanocomposite rheology [18], although the polymer used here has lower molecular weight, and hence viscosity. The PDMS-PDPS copolymer matrix offers the advantage that samples may be prepared and studied at room temperature. In addition, its molecular weight is sufficiently low that it is essentially a viscous liquid; all non-Newtonian rheology may thus be attributed to the dispersed clay particles.

Dispersions were prepared by melt mixing by hand. Organically modified montmorillonite dispersions were prepared at two

loadings: 8 and 15 wt% of organically modified clay (approximately 5.6 and 10.5 wt%, or 2.3 and 4.5 vol% inorganic content, respectively). In addition to X-ray scattering measurements of particle orientation under shear, these dispersions were subjected to extensive rheological testing. A single fluorohectorite dispersion, prepared at 12 wt% loading of organoclay (8.4 wt%, 3.1 vol% inorganic content), was subjected to somewhat more limited X-ray scattering experiments. No complementary rheological testing was performed on this sample. Thus, the montmorillonite dispersions are the primary focus of this report. X-ray data presented below confirm that these melt-mixed samples are in an intercalated state, exhibiting a strong diffraction peak associated with the layered tactoid structure. The *d*-spacings in the montmorillonite and flurohectorite samples are 3.7 and 3.1 nm, respectively. Examination of WAXD peak width and application of the Scherrer equation suggests tactoids of roughly 7–10 layers, implying thicknesses in the range of 25–40 nm, largely independent of concentration. Quantitative analysis of TEM images has often been used to obtain a detailed picture of clay tactoid morphology in solid nanocomposite samples [52–54]. Such studies generally show broad distributions of particle thickness and aspect ratio in nanocomposites. Since the matrix in these dispersions is a viscous fluid, such methods are inaccessible to us, although our samples are likely similarly heterogeneous. While detailed characterization of particle shape distributions is not possible, we may still definitively conclude that (i) these experiments reflect orientation of layered clay tactoids, since we analyze anisotropy in the first-order diffraction peak arising from internal particle layering, and, (ii) that the tactoids are anisotropic in shape (i.e. disk-like), since isotropic particles would not be orientable in shear flow.

### 2.2. Mechanical rheometry

Rheological testing of the montmorillonite dispersions was performed at ambient conditions using an ARES controlled strain rheometer (Rheometrics Scientific), with 50 mm cone and plate fixtures (cone angle = 0.04 rad).

### 2.3. X-ray scattering

X-ray scattering studies of shear-induced particle orientation were performed using a custom annular cone and plate shear cell that facilitates measurements of fluid structure in the 1–2 (flow-gradient) plane of shear flow by sending the incident beam along the 3 (vorticity) axis [55]. Bending magnet radiation (beam line 5BM-D of the Advanced Photon Source) was selected at 25 keV using a double-crystal monochromator. The high energy reduces absorption associated with the long X-ray path length through the sample (~1 cm), and reduces the angle at which diffraction from the layered clay occurs, ensuring that scattered x-rays exit the shear cell unimpeded. Two-dimensional (2D) scattering patterns were collected at a pixel resolution of 512 × 512 using a CCD detector (Mar) at a sample-detector distance of 91 cm. Accounting for both exposure and readout, the maximum rate at which images were collected was approximately 0.25 frames/sec; longer exposures (and correspondingly slower frame rates) were also used.

X-ray scattering patterns provide direct evidence of shear-induced anisotropy in the 1–2 plane (Fig. 1). In both montmorillonite and fluorohectorite dispersions, diffraction from the layering of the clay sheets leads to a well-defined peak as a function of scattering angle. For a one-dimensional layered system, diffraction spots in reciprocal space are concentrated along the direction normal to the layers. In a dispersion of layered clay particles with random orientation distribution, the first-order diffraction spot would be isotropically spread over a spherical surface in reciprocal

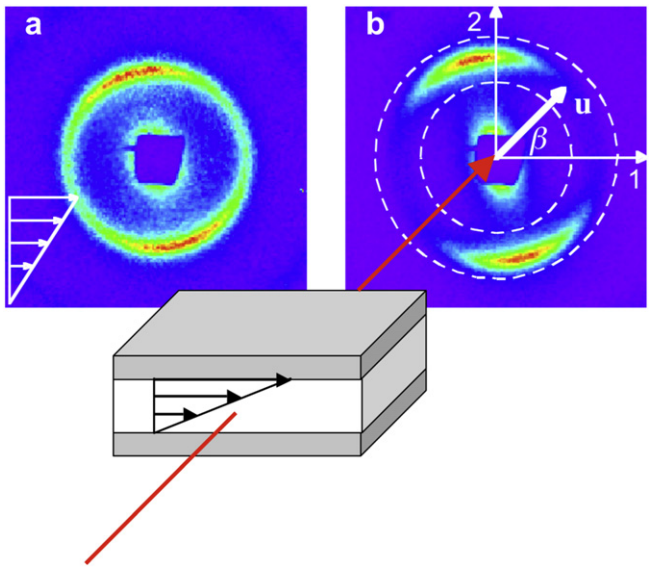


**Fig. 1.** Representative 2D X-ray scattering patterns collected in the 1–2 plane of shear flow, at a shear rate of 0.1 $s^{-1}$ in (a) the 8 wt% montmorillonite dispersion, and (b) the 12 wt% fluorohectorite dispersion. Dashed curves in part (b) illustrate the range of scattering angles used to extract azimuthal intensity scans, $I(\beta)$. The diffraction peak positions in parts (a) and (b) are, respectively, at $q = 1.7$ and 2.0 $nm^{-1}$. For part (b), the cartoon illustrates the spatial relationships between the sheared sample, the incident X-ray beam and the 2D detector. A complete description of the annular cone and plate shear cell used in this work may be found in Ref. [55].

space. In a 2D scattering experiment, the intersection in reciprocal space of this spherical shell of scattered amplitude with the Ewald sphere [56] (the locus of all experimentally realizable scattering vectors) would produce an isotropic ring of scattered intensity in the 2D pattern. When, as in these experiments, the scattering angles are relatively small, reciprocal space is sampled roughly in a plane perpendicular to the incident beam direction (here, the 1–2 plane of shear flow). As a result, scattering observed in Fig. 1 represent contributions from those clay particles whose normals lie (approximately) in the 1–2 plane. Each such particle contributes its diffracted intensity along the direction of its normal. Thus, the azimuthal dependence of the scattered intensity in Fig. 1 provides a direct representation of a 1–2 plane 'slice' of the particle orientation distribution function during shear. In these patterns, the higher scattered intensity observed along the vertical direction indicates—as expected—that particles generally 'lie down' flat in the shear flow, with normals pointing (roughly) along the gradient direction. However, it is clear that the direction of maximum particle orientation is rotated away somewhat from the flow direction, manifested in the fact that the peak in the azimuthal distribution of scattered intensity is rotated counter-clockwise away from the 2-axis. Comparing patterns from montmorillonite (Fig. 1a) and fluorohectorite (Fig. 1b) dispersions, the latter exhibits a higher concentration of scattered intensity in the azimuthal direction, reflecting a higher degree of particle orientation (the fluorohectorite tactoids have higher aspect ratio than the montmorillonite particles).

Here we analyze the azimuthal dependence of the layer diffraction intensity in such 2D patterns to quantify the degree of particle orientation under shear. The patterns in Fig. 1 also exhibit an anisotropic feature at small angles (corresponding to larger length scales); this is attributed to small-angle scattering arising from the anisotropic shape of the disk-like clay particles. It is also possible to extract measures of flow-induced orientation from small-angle X-ray scattering measurements, although this is not pursued here. For exfoliated nanocomposites, in which the

wide-angle diffraction peak from the inter-layer spacing disappears, small-angle scattering is the only route available.

Quantitative analysis of 2D scattering patterns begins with extraction of an azimuthal scan of intensity averaged over a narrow range of scattering angle enclosing the layer diffraction peak (Fig. 1b). This step is performed using the analysis program Fit2D [57]. Each point on such an azimuthal scan may be represented by a unit vector, **u** (as discussed above, **u** also defines the orientation of those particles that contribute to scattered intensity at a given location on the azimuthal scan). We characterize the particle orientation state by calculation of the second moment tensor **uu**, weighted by the azimuthal intensity distribution, $I(\beta)$ [58]:

$$\langle \mathbf{uu} \rangle = \begin{pmatrix} \langle u_1 u_1 \rangle & \langle u_1 u_2 \rangle \\ \langle u_1 u_2 \rangle & \langle u_2 u_2 \rangle \end{pmatrix} = \begin{pmatrix} \langle \cos^2\beta \rangle & \langle \cos\beta \sin\beta \rangle \\ \langle \cos\beta \sin\beta \rangle & \langle \sin^2\beta \rangle \end{pmatrix}, \quad (1)$$

where, using the 11-component as an example, average quantities are computed according to:

$$\langle \cos^2\beta \rangle = \frac{\int_0^{2\pi} \cos^2\beta I(\beta) \mathrm{d}\beta}{\int_0^{2\pi} I(\beta) \mathrm{d}\beta}. \quad (2)$$

The normalization in equation (2) compensates for possible variations in incident beam intensity from one image to the next.

A compact measure of the degree of particle orientation (which we call an anisotropy factor, *AF*) is given by the difference in the principal values of $\langle \mathbf{uu} \rangle$:

$$AF = \sqrt{(\langle u_1 u_1 \rangle - \langle u_2 u_2 \rangle)^2 + 4\langle u_1 u_2 \rangle^2}. \quad (3)$$

Defined in this way, *AF* ranges from 0 for the case of a random distribution of orientation, to 1 for the case of perfect orientation, where all diffracted intensity is concentrated in a particular direction in the azimuthal scan. As such, *AF* is functionally similar to the Hermanns orientation parameter, $\langle P_2 \rangle$, frequently used to characterize orientation in polymers [56]. Techniques to compute $\langle P_2 \rangle$ from 2D scattering data require an assumption that the underlying orientation distribution is uniaxially symmetric. Since we sample only a single 'slice' of the particle orientation distribution in these experiments, there is no way to assess its symmetry; however, shear flow will, in general, *not* promote uniaxially symmetric orientation distributions. For this reason, we favor the second moment tensor approach used here, which characterizes orientation without imposing any further assumptions.

The average particle orientation *direction* within the 1–2 plane may be determined from the principal axes of $\langle \mathbf{uu} \rangle$:

$$\chi = \frac{1}{2}\tan^{-1}\left(\frac{2\langle u_1 u_2 \rangle}{\langle u_1 u_1 \rangle - \langle u_2 u_2 \rangle}\right), \quad (4)$$

where $\chi$ represents the angle measured counter-clockwise from the flow direction to the average orientation direction of the particles' long axes.

## 3. Results

### 3.1. Basic rheology

Small-amplitude oscillatory shear of the montmorillonite dispersions in the linear viscoelastic regime reveals solid-like character typically observed in polymer–clay nanocomposites (Fig. 2).

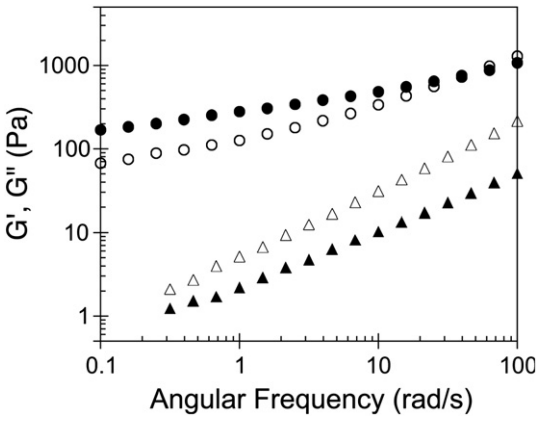


**Fig. 2.** Linear viscoelasticity measured in 8 wt% (triangles) and 15 wt% (circles) montmorillonite dispersions after prolonged relaxation. Filled symbols represent storage modulus, $G'$, while open symbols represent loss modulus, $G''$.

The more highly concentrated (15 wt%) dispersion nearly shows a plateau in storage modulus, with $G' > G''$ at low frequencies. The lower concentration (8 wt%) dispersion exhibits less solid character, although the $G'$ data show signs of 'flattening out' at lower frequencies (experiments could not be extended to lower frequencies due to limitations in torque sensitivity). Recall that the polymer matrix used here has no measurable viscoelasticity; thus, all elastic character present in these samples is due to the dispersed particles. In these samples, clear solid-like rheological signatures are only found at rather high loadings relative to other polymer–clay systems. However, we note that prior studies of clay dispersions in PDMS-PDPS copolymers also showed relatively modest enhancements to viscoelasticity except at high loadings [18].

Comparison of steady shear viscosity to complex viscosity (recast from the linear viscoelastic data in Fig. 2) demonstrates failure of the Cox-Merz rule in these montmorillonite dispersions (Fig. 3). The steady viscosity of the 8 wt% sample exhibits shear thinning at low rates, giving way to nearly Newtonian behavior at higher rates. While a yield stress is not found, the shear thinning at low rates is consistent with the solid-like character revealed by linear viscoelastic testing. The more concentrated 15 wt% sample shows a higher viscosity and much more pronounced shear thinning over the investigated range of shear rates.

### 3.2. Orientation in steady shear flow

X-ray experiments on the clay dispersions were typically performed following various transient flow protocols. Fig. 4 illustrates the time-dependent response of anisotropy factor and orientation angle measured in the 8 wt% montmorillonite dispersion during a representative shear flow reversal and cessation experiment. We generally find that flow-induced orientation does not completely relax; thus, the initial condition upon flow inception depends on the prior flow history. After an initial transient, *AF* and $\chi$ settle into steady state values. (For the experiment in Fig. 4, the first period of shear is taken to be in the negative direction, hence the orientation angle is negative.) Upon reversal, $\chi$ changes sign, and, following a short transient period, settles into a new steady state equal in magnitude but opposite in sign to that during pre-shearing. Following reversal, the anisotropy factor shows a transient undershoot, followed by damped oscillations before it, too, resumes its prior steady state value. Upon flow cessation, the anisotropy factor relaxes partially (but far from completely) accompanied by a small drift in $\chi$ to smaller values. Each of these features is discussed in greater detail in subsequent sections.

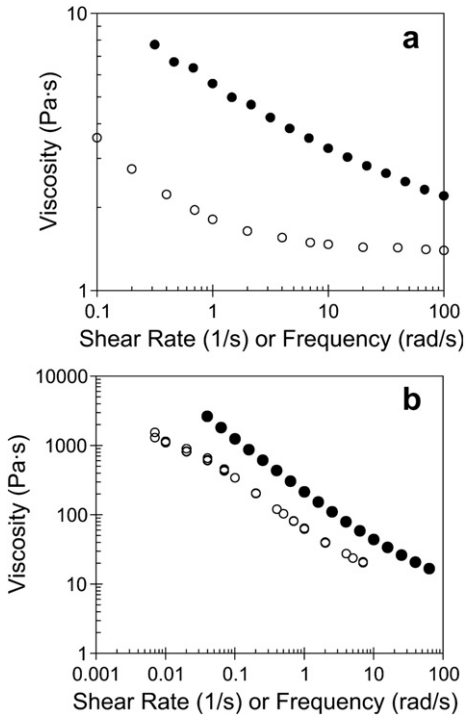


**Fig. 3.** Steady (○) and complex (●) viscosity measured in (a) the 8 wt% montmorillonite dispersion, and (b) the 15 wt% montmorillonite dispersion.

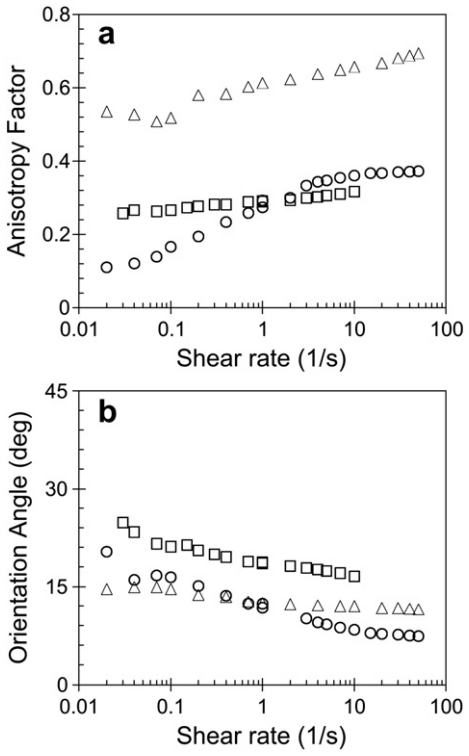


**Fig. 5.** Steady state orientation response of clay dispersions in shear flow. (a) Anisotropy factor and (b) orientation angle measured in the 8 wt% montmorillonite dispersion (○),15 wt% montmorillonite dispersion (□), and 12 wt% fluorohectorite dispersion (△).

Steady state values of anisotropy factor and orientation angle are computed from such time-dependent data by averaging *AF* and $\chi$ data once steady conditions have been achieved. Data from experimental segments with negative shear rates are included by changing the sign of the orientation angle. Steady state data reveal significant levels of flow-induced orientation in these dispersions (Fig. 5). In all cases, a finite, positive orientation angle in the 1–2 plane is observed. As anticipated from the 2D X-ray scattering patterns in Fig. 1, the flurohectorite dispersion shows significantly higher degrees of shear-induced orientation than the montmorillonite samples. In the fluorohectorite dispersion, both *AF* and $\chi$ vary rather weakly with increasing shear rate, with a gradual increase in the degree of particle orientation, and a gradual decrease in the orientation angle (indicating particle alignment closer to the flow direction). Conversely, in the 8 wt% montmorillonite sample, the degree of particle orientation changes significantly between shear rates of 0.1 and 10 $s^{-1}$ before reaching an apparent plateau at high rates. Note that a finite degree of particle orientation is observed even at the lowest shear rates studied. In parallel with the increasing anisotropy in the 8 wt% sample, the orientation angle progressively decreases from ~20° at low rates to ~6° at high rates. Of the three dispersions, the orientation state in this 8 wt% sample is the most 'responsive' to changes in shear rate. In the more concentrated 15 wt% sample, both the degree and direction of orientation change significantly less as a function of shear rate. Interestingly, at high shear rates the 8 wt% sample exhibits higher anisotropy, with particles oriented closer to the flow direction, than observed in the 15 wt% sample.

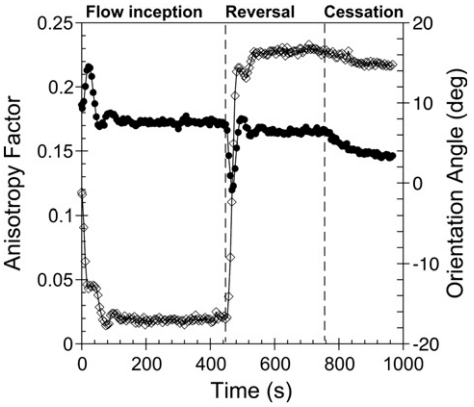


**Fig. 4.** Orientation response measured in a representative time-dependent shear flow reversal and cessation experiment in the 8 wt% montmorillonite dispersion, at a shear rate of 0.1 $s^{-1}$. Anisotropy factor (●) and orientation angle (○) *vs.* elapsed time during shear flow inception, following reversal, and upon shear flow cessation.

### 3.3. Shear flow reversal

The oscillatory response to flow reversal observed in the 8 wt% dispersion in Fig. 4 is also found at other shear rates (Fig. 6). Oscillations in *AF* and $\chi$ scale with applied shear strain, and are quickly damped out such that steady state conditions are re-established after ~15 strain units. Indeed, most particle reorientation from the initial steady state orientation condition in the negative flow direction is accomplished quite quickly, within ~5 strain units (Fig. 6b). Measurements of shear stress in the 8 wt% dispersion do not exhibit oscillatory character (Fig. 7). Upon reversal, the shear stress very rapidly changes sign, but does not immediately attain its steady state value. Rather, over a period of ~4–5 strain units, the stress gradually approaches steady state from an initial value of (depending on prior shear rate) 70–85% of its steady value.

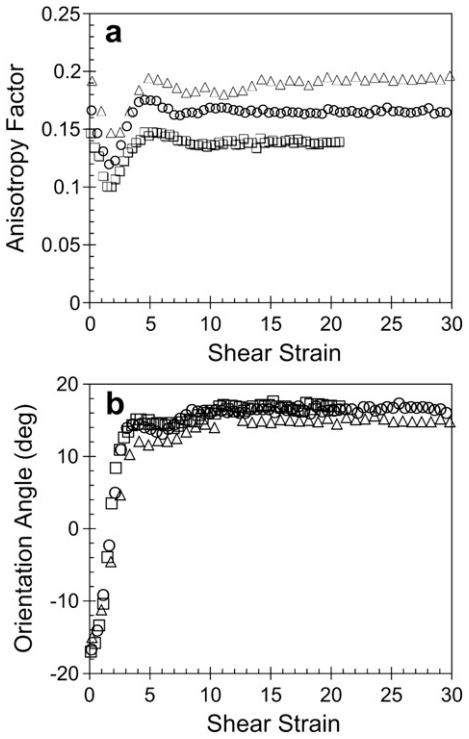


**Fig. 6.** Transient orientation response of the 8 wt% montmorillonite dispersion upon flow reversal. (a) Anisotropy factor and (b) orientation angle vs. shear strain following reversal, at shear rates of 0.07 (□), 0.1 (○) and 0.2 $s^{-1}$ (△).

The other clay dispersions do not exhibit clear signatures of oscillatory structural dynamics upon flow reversal (Fig. 8). Rather, the anisotropy factor shows a single pronounced undershoot as the orientation state evolves towards the steady state appropriate to the new steady state value. Both *AF* and $\chi$ (see Figure S.1, supplemental information) again scale with shear strain. While the transient response is completed quickly in the 15 wt% montmorillonite sample, it persists longer in the 12 wt% fluorohectorite dispersion.

### 3.4. Flow cessation

The 8 wt% montmorillonite dispersion shows significant, but partial relaxation of flow-induced orientation upon cessation of

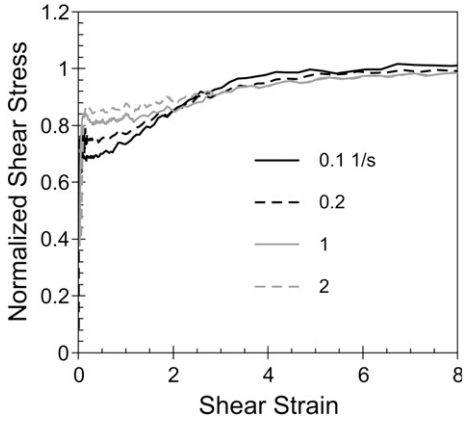


**Fig. 7.** Shear stress, normalized by its steady state value, measured as a function of shear strain in the 8 wt% montmorillonite dispersion following reversal of shear flow at indicated shear rates.

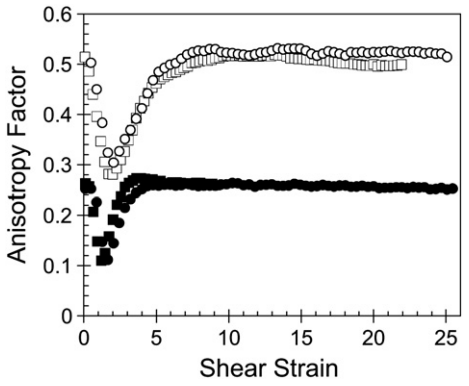


**Fig. 8.** Transient orientation response of the 15 wt% montmorillonite dispersion (filled symbols) and the 12 wt% fluorohectorite dispersion (open symbols) to flow reversal, at shear rates of 0.07 (□,■) and 0.1 $s^{-1}$ (○,●).

shear flow (Fig. 9). When the initial shear rate is low, there is negligible relaxation of orientation, and correspondingly no change in orientation angle. As shear rate increases (accompanied by an increase in the steady state anisotropy during flow), the particle orientation relaxes to an increasing degree, although we never observe *AF* to drop below the value of ≈0.1 observed during shear at low rates. Due to constraints on available synchrotron beam time, the duration of most relaxation experiments was modest. However, one relaxation experiment in the 8 wt% dispersion was extended to 5000 s and, again, showed a persistent fraction of flow-induced orientation that did not relax (Figure S.2). Orientation

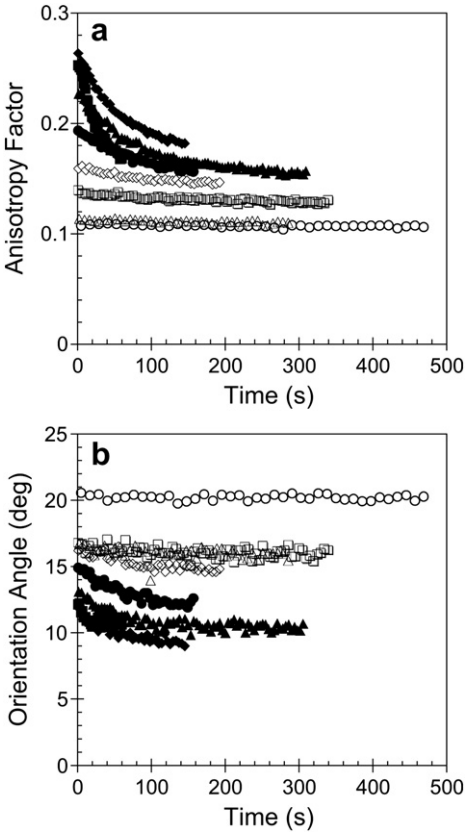


**Fig. 9.** Transient orientation response of the 8 wt% montmorillonite dispersion upon flow cessation. (a) Anisotropy factor and (b) orientation angle *vs.* time following shear at rates of 0.02 (○), 0.04 (△), 0.07 (□), 0.1 (◇), 0.2 (●), 0.4 (▲), 0.7 (■) and 1 $s^{-1}$ (◆).

angle also evolves somewhat towards smaller values during relaxation from higher rates (Fig. 9b). In the 8 wt% montmorillonite dispersion, the observed relaxation phenomena occur on time scales of 10–100 s of seconds.

As discussed in Section 1, structural evolution during relaxation may be probed via mechanical rheological testing. In the 8 wt% montmorillonite dispersion, steady shearing induces a dramatic drop in the dynamic modulus relative to that measured in a well-relaxed state (Fig. 10). The relative drop in $G'$ is much larger than that in $G''$, demonstrating that shear is particularly effective at suppressing the dispersion's elastic character. The moduli recover over an extended period, and, after nearly $10^5$ s, appear to approach limiting values. The degree to which $G'$ and $G''$ are suppressed and the kinetics of their recovery are largely independent of the previously applied shear rate.

Interrupted shearing protocols are also frequently used to interrogate structural evolution following flow cessation. In the 8 wt% montmorillonite dispersion, a stress overshoot develops upon resumption of shear flow as the rest period is increased from 5 to 1200 s (Fig. 11a). For short delay times, the stress response is rather different depending on whether shear flow is resumed in the same or the reversed direction (Fig. 11b). When flow is in the same direction, the stress rapidly resumes its prior steady state, but, when sheared in the opposite direction, the initial transient closely resembles that seen in shear reversal without delay time (Fig. 7). Conversely, for long delay times, a substantial stress overshoot is seen, regardless of whether the pre-shearing was in the same or opposite direction, although the stress response continues to differ depending on whether flow was reversed following the delay period.

In X-ray scattering experiments, neither the 15 wt% montmorillonite dispersion nor the 12 wt% fluorohectorite dispersion exhibit any measurable relaxation in anisotropy factor or orientation angle upon cessation of steady shear flow (Figure S.3). Further evidence of the lack of orientation relaxation in the 15 wt% montmorillonite sample is provided in the context of LAOS experiments discussed in the following section. This sample does, however, still exhibit structural evolution upon flow cessation, as $G'$ and $G''$ measurements show time-dependent behavior very similar to that observed in Fig. 10 (Figure S.4, [59]).

### 3.5. Large-amplitude oscillatory shear

At low frequencies, the use of synchrotron radiation provides sufficient time resolution to probe the orientation dynamics *within* individual cycles of large-amplitude oscillatory shearing (Fig. 12). As the flow direction cycles back and forth, the orientation angle changes sign abruptly, while the anisotropy factor undergoes periodic transient dips, twice per oscillation cycle. While fine details of the orientation response are revealed in these time-resolved data, such results may only be obtained at very low frequencies. For measurements at higher frequencies, where time-resolution is not possible, it is important to choose exposure times

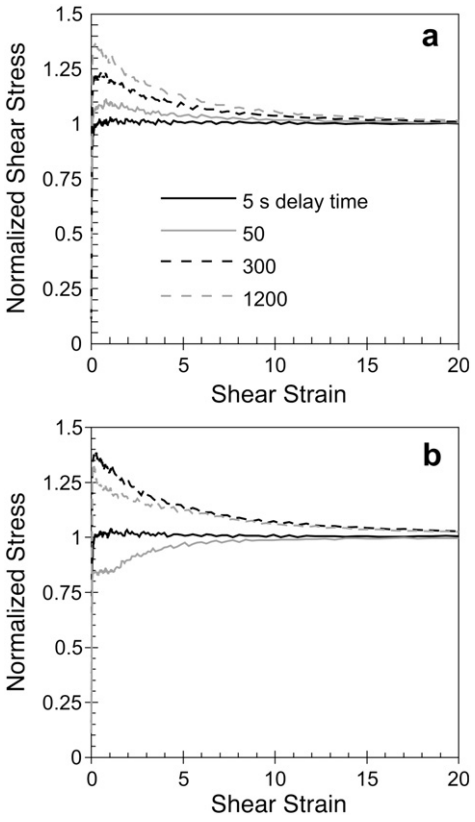


**Fig. 11.** Transient shear stress, normalized by steady state value, measured as a function of shear strain in the 8 wt% montmorillonite dispersion following: (a) interruption in steady shearing at a rate of 1 $s^{-1}$, with indicated delay time; (b) interruption in steady shear shearing (black) or shear flow reversal (gray) at a rate of 1 $s^{-1}$, with delay time of 5 (solid) or 1200 s (dashed).

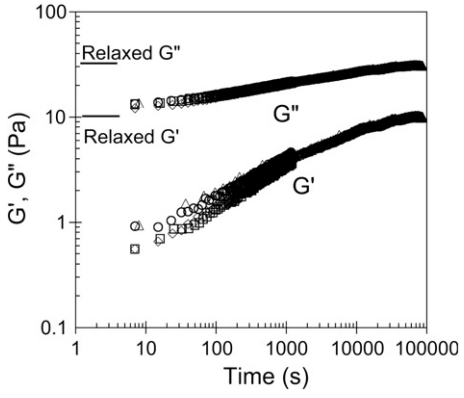


**Fig. 10.** Temporal evolution of storage ($G'$) and loss ($G''$) moduli measured in the 8 wt% montmorillonite dispersion following cessation of shear flow at rates of 0.1 (○), 0.5 (□), 1 (△) and 5 $s^{-1}$ (◇). Measurement frequency = 10 rad/s.

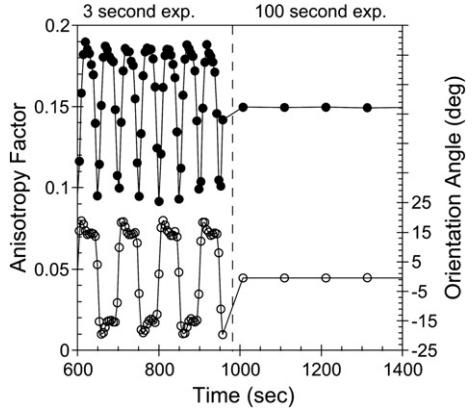


**Fig. 12.** Transient orientation response of the 8 wt% montmorillonite dispersion to large-amplitude oscillatory shear flow, at frequency = 0.01 Hz and strain = 200%. Anisotropy factor (●) and orientation angle (○) vs. time. During the first portion of the experiment, short exposure times allow measurement of the orientation dynamics within cycles of oscillation, while during the latter portion of the experiment, a longer exposure time probes the orientation state time-averaged over one oscillation cycle.

that average over a full cycle (or integral number of cycles) of oscillation. Because the orientation state changes significantly within each cycle, any other choice would lead to ill-defined results that depend on the particular phase of an oscillation cycle sampled during exposure. This principle is illustrated in Fig. 12. Part way through this experiment, the image exposure time was change from 3 s (permitting time-resolved data) to 100 s (which averages orientation state over a full oscillation cycle). Due to the symmetry of the applied LAOS, the orientation angle averages out to zero, while the anisotropy factor measured by this procedure is reduced to a single number characteristic of the time-averaged degree of orientation present under these particular flow conditions. All remaining results in this section are expressed in terms of such time-averaged quantities.

The impact of LAOS strain magnitude on clay orientation is well demonstrated by a sequence of LAOS shearing experiments performed on the 15 wt% montmorillonite sample at a frequency of 0.1 Hz (Fig. 13). Upon inception of the first LAOS segment (100% strain), the time-averaged anisotropy factor quickly reaches a steady value, while the time-averaged orientation angle approaches zero, as expected. Upon termination of this segment of LAOS, the anisotropy factor abruptly drops. This is not relaxation *per se*; rather, when the flow stops, the sample is frozen in a particular orientation state appropriate to that point in the oscillation cycle. For the same reason, upon flow cessation the orientation angle jumps to a nonzero value, since at any particular point in an oscillation cycle the orientation angle will most likely *not* be zero (recall Fig. 12). Resumption of LAOS, now at a strain of 150%, quickly returns the (time-averaged) orientation angle to zero, and leads to a larger anisotropy factor than seen at 100% strain. At the second flow cessation, *AF* and $\chi$ are again 'frozen' at values characteristic of that particular point in the oscillation cycle, in this case with a relative large anisotropy, and large positive orientation angle. The next segment of LAOS employs a smaller strain of 50%. While the time-averaged $\chi$ during LAOS should be zero, the initial condition for this segment is an orientation state that is oriented sufficiently far away from the flow direction that it takes an extended period of time for LAOS at this smaller strain to progressively rotate the average orientation angle back to the flow direction. During this process, the anisotropy factor is gradually reduced from its initially high value, towards a much smaller value. Thus, relative to the high orientation produced during LAOS and 100 or 150% strain, prolonged LAOS at the smaller strain of 50% actively *degrades* the degree of particle orientation to a smaller value. After another rest period, it is seen that a fourth cycle of LAOS at 150% strain quickly returns *AF* to a large value, and the time-averaged orientation angle to zero. There is excellent reproducibility in the anisotropy factor measured during the two segments in this series conducted at 150% strain. Thus, it appears that there is a well-defined and reproducible orientation state associated with each LAOS flow condition (strain + frequency), although prolonged shearing may be required to realize it in the case of smaller strains.

Within each rest segment in Fig. 13 there is no observable relaxation in either *AF* or $\chi$, mirroring observations of negligible relaxation upon cessation of steady shear flow in the 15% montmorillonite dispersion (Figure S.3). A further test for the presence of (possibly subtle) structural changes during rest periods is presented in Fig. 14. Here the sample was subjected to alternating

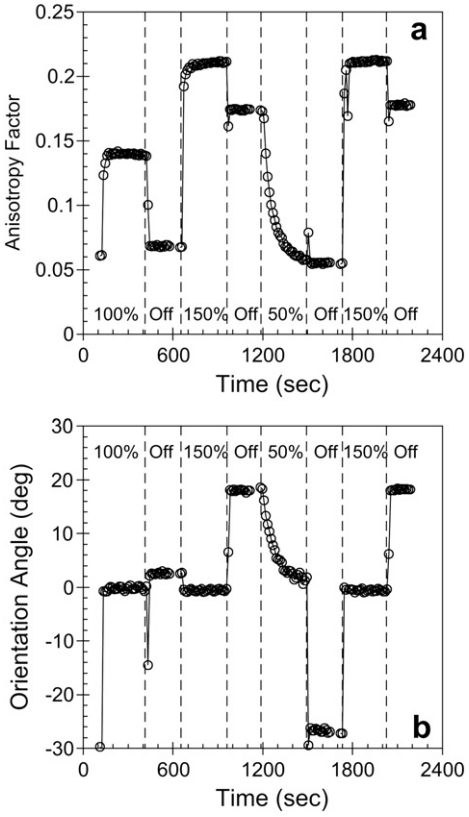


**Fig. 13.** Orientation dynamics of the 15 wt% montmorillonite dispersion during intermittent periods of large-amplitude oscillatory shear flow (frequency = 0.1 Hz) at indicated strain amplitude. (a) Anisotropy factor and (b) orientation angle vs time. X-ray scattering patterns were collected using an exposure time of 10 s, such that, during shear, X-ray data are time-averaged over the oscillation cycle.

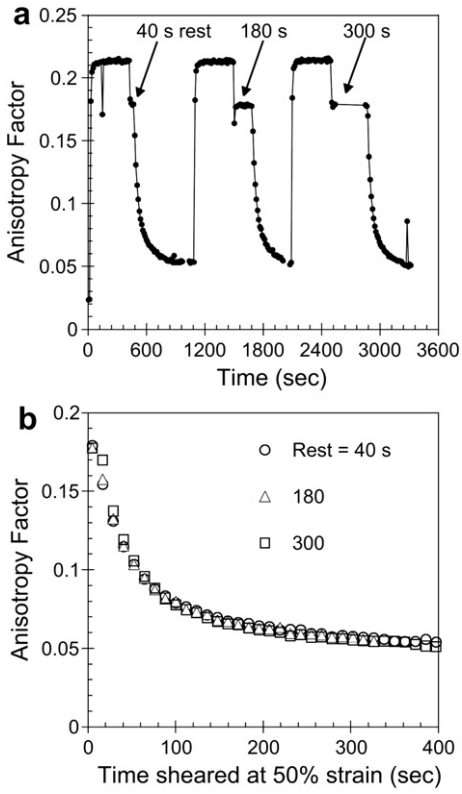


**Fig. 14.** Orientation dynamics of the 15 wt% montmorillonite dispersion during large-amplitude oscillatory shear flow (frequency = 0.1 Hz), alternating between strains of 150% and 50%, with varying periods of resting in between. (a) Anisotropy factor vs time. (b) Comparison of transient anisotropy factor data collected during intervals at 50% strain following three different resting periods.

periods of LAOS at 150% and 50% strain. In between, the sample was allowed to rest for varying duration. Unlike the case in the experiments represented in Fig. 13, here care was taken to stop LAOS at a fixed point during the oscillation cycle at the end of each 150% strain segment, to ensure a reproducible initial condition for the following 50% strain segment. As in Fig. 13, no change in *AF* is observed during the rest interval, while application of LAOS at 50% strain leads to active degradation of the degree of particle orientation. Plotting the transient reduction in *AF* during the 50% strain segments on the same time axis demonstrates that the kinetics of disorientation are remarkably reproducible, and apparently unaffected by the duration of the rest period, further illustrating the lack of structural relaxation in the absence of flow in this sample.

As suggested by Fig. 13, the time-averaged anisotropy factor is a strong function of strain amplitude in the 15 wt% montmorillonite sample; however, it is a relatively weak function of frequency over the range studied (Fig. 15a). Comparing the three different samples used in this study at a fixed strain amplitude of 200% (Fig. 15b), there are general similarities to the shear-rate dependent anisotropy data of Fig. 5. The 12 wt% fluorohectorite dispersion shows the highest degree of particle orientation, and, like the 15 wt% montmorillonite dispersion, shows little sensitivity to frequency. Conversely, the less concentrated 8 wt% montmorillonite dispersion is more responsive to the shear flow conditions, exhibiting a systematic increase in anisotropy factor with increasing frequency. As in the steady state data at high rates, the 8 wt% dispersion exhibits higher orientation than the 15 wt% dispersion at high frequencies.

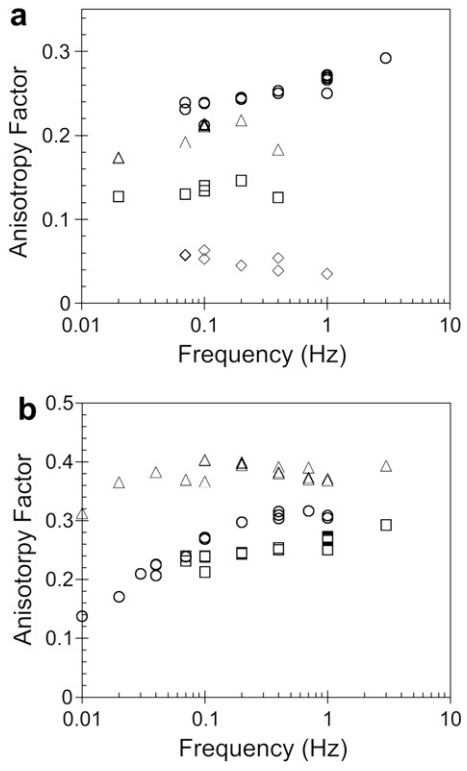


**Fig. 15.** Time-averaged anisotropy factor *vs.* frequency in large-amplitude oscillatory shear. (a) Effect of strain amplitude in the 15 wt% montmorillonite dispersion, measured at strains of 50 (◇), 100 (□), 150 (△) and 200% (○). (b) Comparison of measurements in the 8 wt% montmorillonite (○),15 wt% montmorillonite (□), and 12 wt% fluorohectorite (△) dispersions at a strain amplitude of 200%. See supplemental information for details on the procedure used to time-average low frequency data.

## 4. Discussion

Several studies have noted discrepancies between time scales expected for relaxation of particle orientation via rotational diffusion (which, for highly viscous polymer melt matrices can be extraordinarily long) and times over which structural relaxation is found to occur via interrupted shear protocols [23], modulus evolution [35], or even direct measures of particle orientation [45]. In contrast, the low viscosity of the matrix used in the present work means that rotational diffusion is expected to occur on experimental time scales, at least for the smaller montmorillonite particles. Using their mean diameter of 400 nm, the rotational diffusivity ($D_r = 3k_BT/4\eta d^3$ for disk-like particles of diameter $d$ in a matrix with viscosity $\eta$) is estimated to be 0.035 $s^{-1}$. Following Mobuchon et al. [29], in this calculation we have used the quasi-Newtonian viscosity measured at high rates in the 8 wt% dispersion; thus, this estimate should only be relevant to this sample, which will be the main focus of much of the following discussion. The inverse of this estimated $D_r$ is, indeed, close to the time scales over which partial relaxation of flow-induced orientation is observed to occur in the 8 wt% sample (Fig. 9). Using this estimate, the shear rate range spanned by Fig. 5 corresponds to Peclet number ($Pe = \dot{\gamma}/D_r$) of 0.3–3000. It thus seems clear that rotational Brownian motion should play a role in this dispersion's orientation dynamics.

A useful (if extreme) reference point is the case of a dilute suspension of disk-like particles. Jeffery [59] solved for the deterministic tumbling motion of an isolated ellipsoidal particle in shear flow in the absence of Brownian motion. In these so-called 'Jeffery orbits', the particle rotation slows down as its long axis passes through the flow direction; this is the mechanism by which shear flow is capable of inducing net alignment of non-spherical particles. The influence of rotary Brownian motion in dilute suspensions has received both theoretical [60] and experimental [61] attention. Despite the continuous rotation of individual particles, even small amounts of Brownian motion will disrupt the deterministic character of Jeffery orbits, and lead to a steady state in the particle orientation distribution. Such a steady state orientation distribution, $\psi(\mathbf{u})$, may be characterized by its second moment tensor: $\langle\mathbf{uu}\rangle = \int \mathbf{uu}\psi(\mathbf{u})d\mathbf{u}$ (in the following $\mathbf{u}$ is taken to be a unit vector describing the symmetry axis of a given ellipsoidal particle), which may be computed from:

$$\frac{D}{Dt}\langle\mathbf{u}\rangle = \boldsymbol{\omega}^T\cdot\langle\mathbf{uu}\rangle + \langle\mathbf{uu}\rangle\cdot\boldsymbol{\omega} + \lambda(\mathbf{D}\cdot\langle\mathbf{uu}\rangle + \langle\mathbf{uu}\rangle\cdot\mathbf{D} - 2\langle\mathbf{uuuu}\rangle : \mathbf{D}) - 6D_r\left(\langle\mathbf{uu}\rangle - \frac{1}{3}I\right). \quad (5)$$

In this expression $\mathbf{D}$ is the rate of deformation tensor, $\boldsymbol{\omega}$ is the vorticity tensor, $\mathbf{I}$ is the unit tensor, and $\lambda$ is a geometric parameter determined by particle shape. For ellipsoids of revolution, $\lambda = (p^2-1)/(p^2+1)$, where $p$ is the particle aspect ratio ($p > 1$ for prolate ellipsoids; $p < 1$ for oblate ellipsoids, the case of interest here).

The 8 wt% dispersion of particular interest in the present discussion is obviously not dilute. In concentrated dispersions, particles will influence each other's motions via hydrodynamic interactions and collisions. An approximate treatment of such interparticle interactions was introduced by Folgar and Tucker [62], and has been widely employed in modeling short fiber composite processing. Folgar and Tucker argued that particle interactions perturb Jeffery orbits, and thus act as an effective rotational diffusion process with a diffusivity that is proportional to the shear rate: $C\dot{\gamma}$. $C$ is an interaction coefficient that would, for instance, be expected to increase with particle concentration. The Folgar–Tucker model is commonly applied to non-Brownian dispersions, but if we assume

that rotational diffusion and the effective diffusion process due to particle interactions act in parallel, then $D_r$ in equation (5) may be replaced by:

$$D_{r,eff} = [D_r + C\dot{\gamma}] \quad (6)$$

Equations (5) and (6) provide the simplest framework for considering the combined influence of Brownian motion and interparticle interactions on the orientation dynamics of disk-like particle dispersions. For comparison to experimental orientation data in the 1–2 plane, equations (3) and (4) may be used to compute measures of anisotropy and orientation angle in the computed particle orientation distribution. Solution of equation (5) requires use of a closure approximation for the 4th-order moment tensor. Since our interest here is limited to qualitative behavior, we have adopted the simplest quadratic closure approximation.

In the absence of interparticle interactions ($C = 0$), the orientation dynamics predicted by equation (5) follow expectations for dilute Brownian dispersions (Fig. 16). As $Pe \to 0$, rotational diffusion renders the orientation distribution isotropic ($(AF \to 0)$), and the orientation angle approaches 45°, the principal straining axis of shear flow. Conversely, for $Pe \to \infty$ anisotropy is predicted to saturate, while $\chi$ approaches 0°. While the 8 wt% data in Fig. 5 show trends in qualitative agreement with these predictions, there are discrepancies in both low and high *Pe* limits. At the lowest shear rates studied, *AF* fails to reach 0, and $\chi$ remains far smaller than 45°. Conversely, at high rates, although *AF* appears to saturate, $\chi$ remains at a finite positive value.

The discrepancies at high *Pe* may reflect the influence of interparticle interactions. Since the Folgar–Tucker effective diffusivity is proportional to $\dot{\gamma}$, increasing *C* has the effect of limiting the degree of particle orientation, as well as the extent of alignment along the flow direction, in the $Pe \to \infty$ limit (Fig. 16). Although the more concentrated 15 wt% montmorillonite dispersion does not show any obvious signatures of rotational Brownian motion in either steady shear or relaxation, particle interaction effects may explain differences between the 8 and 15 wt% dispersions in the high shear rate limit. At high *Pe*, both *AF* and $\chi$ approach limiting values that are solely determined by the interaction constant, *C*. The more concentrated montmorillonite dispersion would be expected to have a larger *C*, which would result in (i) lower degree of anisotropy, and (ii) higher orientation angle at high shear rates (Fig. 16), in agreement with experimental observations in Fig. 5.

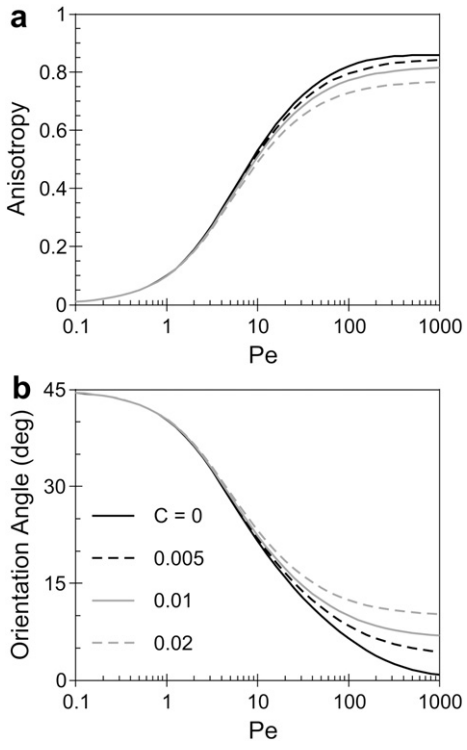


**Fig. 16.** 1–2 plane orientation state predictions according to equations (5) and (6). (a) Anisotropy and (b) orientation angle as a function of Peclet number, computed using a particle aspect ratio $p = 0.2$, and indicated value of interaction constant, *C*.

Equations (5) and (6) provide, at best, a crude representation of orientation dynamics in concentrated disk-like particle dispersions. Recently Meng and Higdon have developed sophisticated algorithms for efficient direct computation of the detailed structure and hydrodynamics of such suspensions [63,64]. Such a simulation approach would have considerable promise to provide detailed insights into the steady and transient orientation data presented here.

The oscillatory structural response observed upon flow reversal (Fig. 6) in the 8 wt% montmorillonite sample can be readily interpreted to arise from the underlying tumbling dynamics of disk-like particles. Although the corresponding mechanical response does not exhibit oscillatory character, there appears to be a close relationship between the structural dynamics and shear stress observed in Fig. 7. In particular, we note that the duration of the transient stress response is very closely correlated with the duration of the primary reorientation reflected in the change in sign of $\chi$ (Fig. 6b). The mechanical data of Fig. 7 span a wide range of shear rates. Over this range, Fig. 5b shows that the orientation angle moves progressively closer to the flow direction at higher rates. As a result, the structural reorientation required upon flow reversal is smaller in extent, providing a direct explanation for why the variation in normalized stress during the reorientation process has a smaller magnitude at higher rates.

Changes in particle orientation induced by flow and during relaxation have frequently been used in interpreting studies of nanocomposite rheology. Figs. 9–11 provide a rare opportunity to test these concepts directly. Observations of anisotropy relaxation in Fig. 9 provide direct evidence of Brownian effects in this dispersion. (The relaxation of orientation angle towards smaller values resembles behavior seen in dilute Brownian dispersions [61], where it is attributed to polydispersity in particle size. Larger particles, which are, on average, aligned closer to the flow direction during shear, relax more slowly. As relaxation proceeds, the average orientation angle is thus increasingly biased towards the smaller values characteristic of the larger particles.) At first glance, the disorientation observed in Fig. 9 provides a satisfying explanation for the recovery of dynamic moduli (Fig. 10), and the development of stress overshoots after rest periods in interrupted shearing flow (Fig. 11), both of which occur on time scales comparable to the orientation relaxation. Closer inspection, however, suggests at best an imperfect correlation between particle orientation and changes in mechanical properties during relaxation. Over the range of shear rates probed in Fig. 10, the steady state degree of particle orientation varies substantially (Fig. 5a). However, there is very little shear rate dependence in the subsequent evolution of linear dynamic modulus. The discrepancy is much starker in the 15 wt% montmorillonite suspension for which *no* relaxation of particle orientation is observed following cessation of either steady shear (Figure S.3) or LAOS (Figs. 13 and 14). Nevertheless, this sample also exhibits recovery of dynamic modulus during relaxation that is very similar to that observed in Fig. 10 (Figure S.4). For this reason, we conclude that recovery of dynamic moduli (and associated solid-like character) following cessation of shear flow primarily arises due to reformation of a mechanically percolated nanoparticle

network, which may or may not occur in parallel with significant changes to the particle orientation state. In a sufficiently concentrated dispersion, we postulate that interparticle associations that are broken during shear are able to reform even in the absence of measurable changes in the average particle orientation state.

Comparison of interrupted shear and interrupted reversal data in Fig. 11b reinforces the role of particle network reformation during the rest period. For short rest periods, in which negligible network formation can occur, the differences in transient response upon flow resumption are directly attributable to the particle reorientation that is necessary upon shear flow resumption in the reversed direction. While there is some relaxation of particle orientation, the data in Fig. 9 make clear that there will *still* be substantial particle reorientation necessary in the interrupted reversal case when flow is resumed after a 1200 s delay. Indeed, the stress transients continue to exhibit differences depending on whether flow is resumed in the same or the reversed direction. In both cases, however, a large stress overshoot is present, which we postulate emerges as a result of particulate network reformation in the quiescent state. (Fractal particle networks have similarly been identified as the source of stress overshoots in polymer–carbon nanotube dispersions [65]). The data of Fig. 11a (and the interpretation described here) closely parallel observations of Vermant et al. in similar testing protocols [38].

Redevelopment of particle network structure may provide an explanation for the failure of the 8 wt% dispersion to relax to a fully random orientation state (Fig. 9). This observation seems closely related to the persistence of finite anisotropy in this dispersion at the lowest shear rates in Fig. 5a. In fact, *none* of the dispersions studied here ever exhibited a random particle orientation distribution, highlighting the role that flow history during sample preparation and loading may have on the structure of nanocomposites during rheological testing. All the dispersions studied here are quite highly concentrated. At sufficient loading, anisotropic disk-shaped particles are expected to form an ordered nematic phase; for instance, Jogun and Zukoski utilized liquid crystal concepts in interpreting rheological data collected on highly concentrated aqueous clay dispersions [66]. *In situ* measurements of particle orientation could conceivably help determine whether nematic ordering is present. However, in the presence of complicating factors such as particle networks formed due to interparticle associations, it may be hard to draw definitive conclusions. For instance, does the lack of orientation relaxation observed here in the more concentrated dispersions reflect hindered relaxation due to by nanoparticle networks, or does it reflect equilibrium nematic ordering? The existence of strong analogies between the hydrodynamics of anisotropic particles and nematics renders such questions more difficult. For instance, the Folgar–Tucker model of interacting fibers is virtually identical to the Larson–Doi model of polydomain nematics [67,68], and, indeed, the orientation dynamics observed upon flow reversal in Fig. 6 closely resemble experimental observations in tumbling nematic liquid crystalline polymers [55]. Certainly, however, polymer–clay nanocomposites share the trait common to all classes of complex fluids that direct measurements of structural changes during flow provide many useful insights into the origin of complex rheological behavior.

## 5. Conclusions

We have reported *in situ* measurements of particle orientation in sheared dispersions of organically modified montmorillonite and fluorohectorite in a low viscosity polymer melt using synchrotron-based X-ray scattering. Anisotropic 2D diffraction patterns from disk-shaped intercalated clay tactoids allow quantitative analysis of the average degree and direction of particle orientation during shear flow. Due to the low matrix viscosity, effects of rotational diffusion are clearly manifested in a moderately concentrated (8 wt%) montmorillonite dispersion, which shows shear rate-dependent anisotropy factor and orientation angle, and partial relaxation of orientation upon flow cessation. Conversely, a more highly concentrated montmorillonite dispersion and a fluorohectorite dispersion show less rate dependence in orientation state, and no orientation relaxation. In all samples, a finite average particle orientation angle relative to the flow direction is observed at all shear rates; the inability of shear to induce truly 'parallel' alignment is attributed to interparticle interactions. The flurohectorite sample shows a higher level of orientation, consistent with its higher aspect ratio particles. Similar trends in orientation are observed as a function of frequency in large-amplitude oscillatory shear.

Connections between flow-induced particle orientation and rheology were explored. Particle reorientation upon reversal of shear flow direction is accompanied by a transient feature in shear stress measurements. However, characteristic oscillatory structural dynamics in the 8 wt% montmorillonite dispersion (attributed to Jeffrey orbit tumbling of disk-like particles) are not manifested in the mechanical response. Application of shear flow suppresses dynamic moduli, which gradually recover following flow cessation. Similarly, interrupted shear testing reveals that stress overshoots during resumption of shear grow with increasing delay time. While these processes occur in parallel with partial relaxation of orientation in the 8 wt% montmorillonite dispersion, similar rheological signatures are present in more concentrated samples that show no relaxation of orientation. For this reason, we concluded that development of increased elastic character in these clay dispersions following flow cessation is primarily associated with redevelopment of particle networks that are disrupted by shear flow.

## Acknowledgments

This work was funded by the NSF-MRSEC program (Grants DMR-0076097 and DMR-0520513) at the Materials Research Center of Northwestern University. L. Dykes acknowledges support from a GEM Fellowship. Support of the Texas Institute for Intelligent Bio-Nano Materials and Structures for Aerospace Vehicles, funded by NASA Cooperative Agreement NCC-1-02038, is gratefully acknowledged by R. Krishnamoorti. We thank the staff of the DuPont-Northwestern-Dow Collaborative Access Team (DND-CAT) at Sector 5 of the Advanced Photon Source for their help with setup and execution of synchrotron experiments, and K. Brinker and S. Rendon for assistance in running the experiments. DND-CAT is supported by the E.I. DuPont de Nemours & Co., the Dow Chemical Company, and the National Science Foundation through Grant DMR-9304725 and the State of Illinois through the Department of Commerce and the Board of Higher Education Grant IBHE HECA NWU 96. Use of the Advanced Photon Source was supported by the U.S. Department of Energy, Basic Energy Sciences, Office of Energy Research, under Contract No. W-31-102-Eng-38.

## Appendix. Supplementary material

Supplementary material related to this article can be found online at doi:10.1016/j.polymer.2010.08.013.

## References

[1] Giannelis EP. Adv Mat 1996;8:29–35.
[2] Alexandre M, Dubois P. Mat Sci Eng R 2000;28:1–63.
[3] Pinnavaia TJ, Beall GW, editors. Polymer–clay nanocomposites. New York: Wiley; 2000.

[4] Mai Y-W, Yu Z-Z, editors. Polymer nanocomposites. Cambridge: Woodhead; 2006.
[5] Giannelis EP, Krishnamoorti R, Manias E. Adv Polym Sci 1999;138:107–47.
[6] Brune DA, Bicerano J. Polymer 2002;43:369–87.
[7] Sorrentino A, Gorrasi G, Tortora M, Vittoria V. In: Mai Y-W, Yu Z-Z, editors. Polymer nanocomposites. Cambridge: Woodhead; 2006. p. 273–96.
[8] Kim H, Macosko CW. Polymer 2009;50:3797–809.
[9] Kojima Y, Usuki A, Kawasumi M, Okada A, Kurauchi T, Kamigaito O, et al. J Polym Sci Part B Polym Phys 1995;33:1039–45.
[10] Ogata N, Jimenez G, Kawai H, Ogihara T. J Polym Sci Part B Polym Phys 1997; 35:389–96.
[11] Varlot K, Reynoud E, Klopper MH, Vigier G, Varlet J. J Polym Sci Part B Polym Phys 2000;39:1360–70.
[12] Kim G-M, Lee D-H, Hoffmann B, Kressler J, Stöppelmann G. Polymer 2000; 42:1095–100.
[13] Fong H, Liu W, Wang C-S, Vaia RA. Polymer 2002;43:775–80.
[14] Bafna A, Beucage G, Mirabella F, Mehta S. Polymer 2003;44:1103–15.
[15] Fornes TD, Paul DR. Polymer 2003;4:4993–5013.
[16] Galgali G, Agarwal S, Lele A. Polymer 2004;45:6059–69.
[17] Krishnamoorti R, Yurekli K. Curr Op Coll Inter Sci 2001;6:464–70.
[18] Krishnamoorti R, Vaia RA, Giannelis EP. Chem Mater 1996;8:1728–34.
[19] Krishnamoorti R, Giannelis EP. Macromolecules 1997;30:4097–102.
[20] Ren J, Silva AS, Krishnamoorti R. Macromolecules 2000;33:3739–46.
[21] Hoffmann B, Dietrich C, Rhomann R, Friedrich C, Mülhaput R. Macromol Rap Comm 2000;21:57–61.
[22] Lim YT, Park OO. Rheol Acta 2001;40:220–9.
[23] Solomon MJ, Asmusallam AS, Seefeldt KF, Somwangthanaroj A, Varadan P. Macromolecules 2001;34:1864–72.
[24] Lee KM, Han CD. Polymer 2003;44:4573–88.
[25] Wagener R, Reisinger TJG. Polymer 2003;44:7513–8.
[26] Zhao J, Morgan AB, Harris JD. Polymer 2005;46:8641–60.
[27] Wang XL, Sun PC, Xue G, Winter HH. Macromolecules 2010;43:354–61.
[28] Galgali G, Ramesh C, Lele A. Macromolecules 2001;34:852–8.
[29] Mobuchon C, Carreau PJ, Heuzey M-C. Rheol Acta 2007;46:1045–56.
[30] Krishnamoorti R, Giannelis EP. Langmuir 2001;17:1448–52.
[31] Krishnamoorti R, Ren J, Silva AS. J Chem Phys 2001;114:4968–73.
[32] Ren J, Krishnamoort R. Macromolecules 2003;36:4443–51.
[33] Xu L, Reeder S, Thopasridharan M, Ren J, Shipp DA, Krishnamoorti R. Nanotechnology 2005;16:5514–22.
[34] Krishnamoorti R, Silva AS. In: Pinnavaia TJ, Beall GW, editors. Polymer–clay nanocomposites. New York: Wiley; 2000. p. 315–43.
[35] Ren J, Casanueva BF, Mitchell CA, Krishnamoorti R. Macromolecules 2003; 36:4188–94.
[36] Treece MA, Oberhauser JP. Macromolecules 2007;40:571–82.
[37] Treece MA, Oberhauser JP. Polymer 2007;48:1083–95.
[38] Vermant J, Ceccia S, Dolgovskij MK, Maffettone PL, Macosko CW. J Rheol 2007;51:429–50.
[39] Letwimolnun W, Vergnes B, Ausias G, Carreau PJ. J Non-Newtonian Fluid Mech 2007;141:167–79.
[40] Zhu YT, Cardinaels R, Mewis J, Moldenaers P. Rheol Acta 2009;48:1049–58.
[41] Chen G, Qi Z, Shen D. J Mater Res 2000;15:351–6.
[42] Okamoto M, Nam PH, Maiti P, Kotaka T, Hasegawa N, Usuki A. Nano Lett 2001;1:295–8.
[43] Schmidt G, Nakatani AI, Butler PD, Karim A, Han CC. Macromolecules 2000;33:7219–22.
[44] Medellin-Rodriquez FJ, Burger C, Hsiao BS, Chu B, Vaia R, Phillips S. Polymer 2001;42:9015–23.
[45] Lele A, Mackley M, Galgali G, Ramesh C. J Rheol 2002;46:1091–110.
[46] Ramsay JDF, Lindner P. J Chem Sos Faraday Trans 1993;89:4207–14.
[47] Brown ABD, Clarke SM, Convert P, Rennie AR. J Rheol 2000;44:221–33.
[48] Jogun SM, Zukoski CF. J Rheol 1999;43:847–71.
[49] Camerel F, Gabriel JCP, Batail P, Painine P, Davidson P. Langmuir 2003;19:10028–35.
[50] Reyna-Valencia A, Deyrail Y, Bousmina M. Macromolecules 2010;43: 354–61.
[51] Mitchell CA, Krishnamoorti R. J Polym Sci Part B Polym Phys 2002;40: 1434–43.
[52] Chavarria F, Paul DR. Polymer 2004;45:8510–5.
[53] Lee H-S, Fasulo PD, Rodgers WR, Paul DR. Polymer 2005;46:11673–89.
[54] Yoo Y, Paul DR. Polymer 2008;49:3795–804.
[55] Caputo FE, Burghardt WR. Macromolcules 2001;34:6684–94.
[56] Roe RJ. Methods of X-ray and neutron scattering in polymer science. New York: Oxford; 2000.
[57] Hammersley A. Web source: http://www.esrf.eu/computing/scientific/FIT2D/.
[58] Cinader DK, Burghardt WR. J Polym Sci Part B Polym Phys 1999;37:3411–28.
[59] Jeffery G. Proc Roy Soc Lond A 1992;102:161–79.
[60] Leal LG, Hinch EJ. J Fluid Mech 1971;46:685–703.
[61] Frattini PL, Fuller GG. J Fluid Mech 1986;168:119–50.
[62] Folgar F, Tucker CL. J Reinforced Plat Comp 1984;3:98–119.
[63] Meng Q, Higdon JJL. J Rheol 2008;52:1–36.
[64] Meng Q, Higdon JJL. J Rheol 2008;52:37–65.
[65] Chatterjee T, Krishnamoorti R. Macromolecules 2008;41:5333–8.
[66] Jogun S, Zukoski CF. J Rheol 1996;40:1211–32.
[67] Larson RG. The structure and rheology of complex fluids. New York: Cambridge; 1998.
[68] Larson RG, Doi M. J Rheol 1991;35:539–63.